Cell Reports
Physical Science

Article

Thermo- vs. electrocatalysis on Fe- and Ru-based cathodes for ammonia synthesis in proton-conducting ceramic cells

Graphical abstract

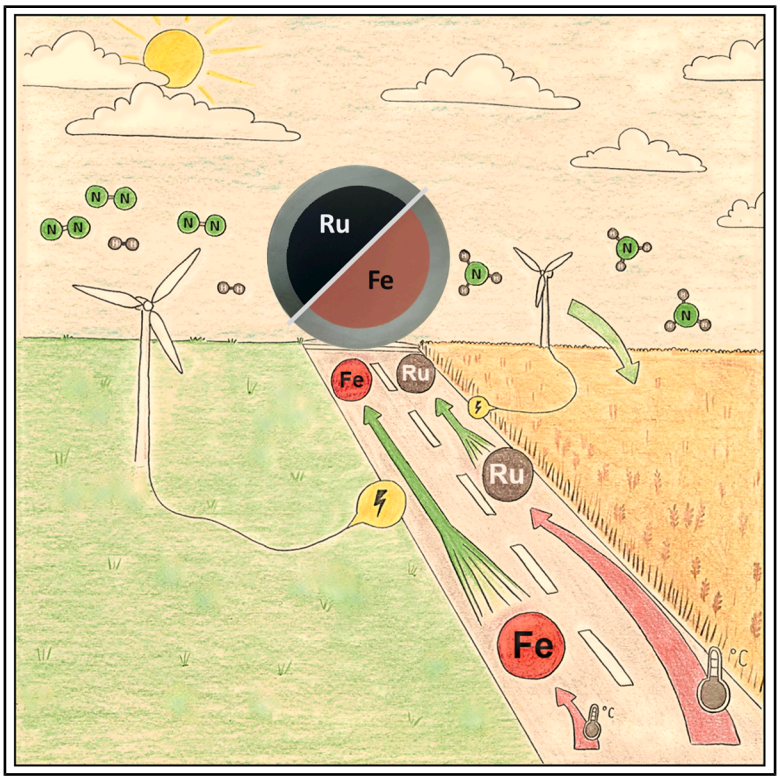

Highlights

- Ru shows higher intrinsic NH_3 synthesis activity than Fe under OCV
- Fe responds more strongly to polarization and approaches Ru performance
- A 12.57 cm^2 active area enables performance testing at enlarged cell scale
- Highest reported NH_3 formation rates for Fe-based PCC electrodes

Authors

Philipp Blanck, Konstantin Elfner, Etienne P. Martin, Daniel Schmider, Robert J. Kee, Julian Dailly, Olaf Deutschmann

Correspondence

julian.dailly@eifer.org (J.D.), deutschmann@kit.edu (O.D.)

In brief

Blanck et al. compare Fe- and Ru-based cathodes for ammonia synthesis in proton-conducting ceramic cells. Although Ru is more active under thermocatalytic conditions, electrical polarization strongly enhances Fe, enabling rates approaching those of Ru and highlighting complementary catalyst strategies for ammonia production under polarization.

Blanck et al., 2026, Cell Reports Physical Science 7, 103482
August 19, 2026
https://doi.org/10.1016/j.xcrp.2026.103482

CellPress

Cell Reports
Physical Science

CellPress
OPEN ACCESS

Article

Thermo- vs. electrocatalysis on Fe- and Ru-based cathodes for ammonia synthesis in proton-conducting ceramic cells

Philipp Blanck,[1,2] Konstantin Elfner,[1] Etienne P. Martin,[2] Daniel Schmider,[2] Robert J. Kee,[3] Julian Dailly,[2,*] and Olaf Deutschmann[1,4,*]

[1]Karlsruhe Institute of Technology (KIT), Institute for Chemical Technology and Polymer Chemistry (ITCP), Engesserstrasse 20, 76131 Karlsruhe, Germany

[2]European Institute for Energy Research (EIfER), Emmy-Noether-Strasse 11, 76131 Karlsruhe, Germany

[3]Colorado School of Mines (CSM), Department of Mechanical Engineering, 1500 Illinois Street, Golden, CO 80401, USA

[4]Lead contact

*Correspondence: julian.dailly@eifer.org (J.D.), deutschmann@kit.edu (O.D.)

https://doi.org/10.1016/j.xcrp.2026.103482

SUMMARY

Electrochemical ammonia synthesis in proton-conducting ceramic cells offers an electricity-assisted alternative to the energy-intensive Haber-Bosch process and may enable decentralized NH_3 production. This study compares the performances of Fe- and Ru-based cathodes with similar catalyst loadings on BCZY721 membranes and an active area of 12.57 cm^2. Under open-circuit voltage (OCV) conditions, Ru exhibited NH_3 synthesis rates nearly two orders of magnitude higher than those of Fe. Under polarization, rates of 5.52×10^{-8} mol cm^{-2} s^{-1} for Ru and 3.03×10^{-8} mol cm^{-2} s^{-1} for Fe were achieved, while increased Ru loading further raised the rate to 7.70×10^{-8} mol cm^{-2} s^{-1} at 475°C. Despite its lower intrinsic activity, Fe showed a substantially stronger relative response to polarization and approached the performance of Ru. These distinct behaviors provide a basis for electrode concepts combining high intrinsic activity with strong polarization responsiveness. Further mechanistic studies are required to clarify the origin of the observed performance differences.

INTRODUCTION

Ammonia (NH_3) is a critically important commodity, predominantly synthesized via the Haber-Bosch process, which requires very high pressure and elevated temperature. The process relies heavily on hydrogen derived from fossil fuels, making it both energy and carbon intensive. The annual NH_3 production of approximately 240 million metric tons consumes approximately 2% (8.6 EJ) of the world's total energy and contributes nearly 1.3% (450 Mt) of global anthropogenic CO_2 emissions.[1]

NH_3 is inherently challenging to synthesize from H_2 and N_2 because of the exceptionally strong N≡N triple bond. The global conversion process ($N_2 + 3H_2 \rightleftharpoons 2NH_3$) is an exothermic mole-reducing reaction that favors high pressure and low temperature. However, at temperatures below ~500°C significant kinetic limitations greatly reduce the NH_3 formation rate. In accordance with Le Chatelier's principle, applying high pressure shifts the equilibrium toward NH_3, a strategy that works efficiently in large-scale industrial Haber-Bosch plants but is difficult to implement in decentralized, renewable-powered systems.

Small-scale, low-pressure NH_3 production offers important advantages, such as reduced transport requirements, compatibility with intermittent renewable energy, and a lower carbon footprint. However, achieving competitive reaction rates while approaching thermodynamic near-equilibrium performance at low temperatures remains a significant kinetic challenge. Electrochemically assisted catalysis can address this limitation by altering catalyst activity and reaction energetics under polarization, thereby facilitating NH_3 formation even at atmospheric pressure.

Electrochemical NH_3 synthesis offers a promising pathway to sustainable NH_3 production, particularly when powered by renewable electricity. In this context, proton-conducting ceramic cells (PCCs) have attracted growing attention.[2–4]

Catalyst performance is crucial to facilitate N_2 adsorption and dissociation, promote the formation of surface intermediates, and suppress competing side reactions such as the hydrogen evolution reaction (HER). Enhancing catalytic performance at temperatures below 500°C is particularly important to achieve equilibrium conversion under mild conditions. In addition to the well-studied palladium (Pd)- and iron (Fe)-based catalysts, ruthenium (Ru) is of interest as a catalyst for NH_3 production using PCCs due to its high thermocatalytic activity.

NH_3 synthesis activity depends on the number of *d* electrons in transition-metal catalysts, with the three most active catalysts (Ru, osmium [Os], and Fe) all possessing seven *d* electrons. Among them, Ru exhibits the highest catalytic activity, delivering the best synthesis rates.[5,6] Ru also holds a near-optimal position

in the Sabatier volcano plot for electrochemical NH_3 synthesis, exhibiting a balanced nitrogen adsorption energy (ΔE_{N^*}) that enables effective N_2 activation while facilitating the desorption of the produced NH_3. Ru's near-optimal catalytic performance, combined with low electrochemical overpotential requirements, makes Ru a promising catalyst for integration into proton-conducting electrochemical systems.[7]

One mechanistic picture proposed for PCCs is the direct participation of transported protons in the hydrogenation of N_2, potentially lowering the barrier associated with N≡N bond activation. However, under typical operating conditions, protons are more likely to recombine into molecular H_2 than to be incorporated directly into NH_3. Alternatively, catalytic activity can be enhanced by polarization-induced modification of the catalyst surface, often discussed in terms of electrochemical promotion of catalysis (EPOC), in which the electric field and ionic transport through the electrolyte alter the catalytic properties of the surface.[8] Previous studies suggest that such surface-promotion effects may contribute substantially to the observed rate enhancement.[9] This interpretation is consistent with isotope-based studies by Li et al., in which the detected NH_3 predominantly reflected the H_2 or deuterium species supplied in the cathode feed, indicating that cathode-side hydrogenation pathways can play an important role and that NH_3 formation does not rely exclusively on protonic species transported through the electrolyte.[10]

The present study investigates and compares the performance of pure Fe and Ru integrated into the cathode of proton-conducting ceramic systems for electrochemically assisted NH_3 synthesis. To ensure a fair comparison, the cell designs and metal loadings were kept as similar as possible, while operating parameters such as temperature, applied cell voltage, and gas flow rate were systematically varied for both systems. By comparing two catalysts with fundamentally different intrinsic catalytic activities and electrochemical responses, the study aims to clarify how catalyst identity influences the balance between thermocatalytic activity and electrochemical promotion in PCC-based NH_3 synthesis. The work is designed as a comparative performance investigation rather than a definitive mechanistic study.

Previous research on protonic ceramic cells for ammonia synthesis

Table 1 presents a comprehensive summary of electrochemical NH_3 synthesis using proton-conducting electrolyte membranes, employing a variety of electrode architectures produced by different methods. In the upper section of Table 1, all active electrodes incorporate Ru either exclusively or in combination with other elements as the catalytic component, while in the lower section, Fe constitutes the main catalytic component. The supplemental information (Table S1) provides additional parameters, such as anode and electrolyte compositions and details of experimental conditions.

The peak values for NH_3 formation rates r_{NH_3} in PCCs reported in the literature are mostly within the order of magnitude of 10^{-9} mol cm^{-2} s^{-1} or below (compare Figure 1), with the exception of the values reported by Li et al. in 2022 at 400°C, which were up to 81.1×10^{-9} mol cm^{-2} s^{-1}.[17]

Comparing NH_3 formation rates with those reported by other authors employing non-noble catalysts, such as Fe alone, the observed rates similarly fall within the decades of 10^{-10} to 10^{-9} mol cm^{-2} s^{-1}.[10,13,26] Notably, Okazaki et al. reported in single-chamber experiments peak formation rates of 17×10^{-9} mol cm^{-2} s^{-1} at 600°C and 11×10^{-9} mol cm^{-2} s^{-1} at 400°C using a pure Fe catalyst.[25,31]

The reactor geometries and material-synthesis methods for the Ru-based catalysts presented in Table 1 vary. Approaches such as solid-state synthesis[11,20,28]; the co-precipitation method[12]; an ethylenediaminetetraacetic acid (EDTA)-citrate complex method[16]; impregnation with $Ru(NO_3)_3$,[13,15] $Ru(NO)(NO_3)_3$,[20] or $Ru(NH_3)_6Cl_3$[17]; radio frequency reactive sputtering[19]; and electrospinning[21] were used with no clear performance trends. However, all results in which the electrode was prepared using the solid-state synthesis method have the lowest r_{NH_3} rates, all falling below 10^{-10} mol cm^{-2} s^{-1}, indicating low activity of the added Ru. Similarly, no clear trends related to electrode fabrication can be identified for the Fe-based electrodes.

In this work, a deliberately straightforward materials integration strategy is employed in which Fe_2O_3 and RuO_2 are incorporated in their oxide form into a well-defined porous electrode backbone via a single thick-film deposition step, thereby avoiding intricate composite syntheses or multistage processing routes.

Furthermore, a specially adapted test bench (Figure 2) enables the electrochemical evaluation of PCCs with an enlarged active area of 12.57 cm^2, corresponding to a 10 to 100 times increase compared with previously reported cells in the field of electrochemical NH_3 synthesis (Table 1). This demonstration of cell level scale-up within this research area, together with the promising performance achieved (compare Table 1), indicates the potential of the presented approach and provides a solid basis for future progress toward practically relevant device dimensions.

RESULTS

An H_2:N_2 ratio of 1:1 was chosen at the cathode, as previous experiments showed that the optimal performance of a comparable Fe electrode occurs near this ratio.[9] For each operating point, the cell was stabilized for at least 10 min before two consecutive samples were collected for NH_3 analysis. The complete experimental campaign for each individual cell extended over approximately 2 weeks. The measured r_{NH_3} were compared with thermodynamic equilibrium values calculated with $DETCHEM^{EQUIL}$ for an inlet gas composition of H_2:N_2 = 1:1 under open-circuit voltage (OCV) conditions.[32] Representative equilibrium NH_3 values for selected operating conditions are provided in Table S2. The influence of the HER on the total gas flow, and the resulting minor increase in the H_2 mole fraction, is not accounted for, as these effects are negligible and only slightly shift the thermodynamic equilibrium toward higher NH_3 values. Consequently, the thermodynamic curves presented in the figures provide a slightly underestimated reference for evaluating how closely the experimental data approach equilibrium.

Fe electrode

For comparison with cells employing pure Ru, a cell incorporating an Fe-based catalyst electrode was studied first. Measurements were conducted at three temperatures, 500°C,

Table 1. Literature on electrochemical NH_3 synthesis utilizing Ru (top) or Fe (bottom) as a catalyst at the cathode

Cathode	Active area (cm^2)	T (°C)	r_{NH_3} ($\times 10^{-9}$ mol cm^{-2} s^{-1})	Reference
Ruthenium-based electrodes				
LSTR40-BCYR	0.79	500	0.005	Otomo et al.[11]
Ni-BCYR	0.79	500	0.53	Kobayashi et al.[12]
BCZYZ/Fe-Ru	0.4	500	2.7	Klinsrisuk et al.[13]
LST-BCYR	0.39	500	0.002	Kosaka et al.[14]
Ni-BCYR	0.39	500	0.011	Kosaka et al.[14]
K-Ru-BCY	0.39	700	0.55	Li et al.[15]
BSTR	0.28	500	1.1	Kim et al.[16]
PBSCF/LDC-Ru	–	400	81.1	Li et al.[17]
PBSCF/Ru	–	400	6.9	Li et al.[17]
Ru/LWO	–	350	8.91	Weng et al.[18]
Ru-$VN_{0.9}$	1.13	600	3.8	Kamitani et al.[19]
Ru-$VN_{1.1}$	1.13	600	1.4	Kamitani et al.[19]
I-Ru-LSCF-BZCYYb1711	0.28	400	0.0514	Chen et al.[20]
I-Ru-BZCYYb1711	0.28	400	0.01	Chen et al.[20]
Ru-LSCF-BZCYYb1711	0.28	400	0.004	Chen et al.[20]
PBSCF-BZCYYb1711/Ru-GDC	0.6	650	4.06	Dang et al.[21]
Ru in BCZY721 backbone	12.57	475	77.0	**This work**
Iron-based electrodes				
BCZYZ/Fe	0.4	400	2.9	Klinsrisuk et al.[13]
BCZYZ/Fe-Pd	0.4	450	4.0	Klinsrisuk et al.[13]
K-Fe-BCY	0.39	700	0.596	Li et al.[15]
Ni-BCZG/Fe+K	0.44	500	0.187	Lei et al.[22]
BZY20/Fe	0.79	500	3.07	Yuan et al.[23]
VN-Fe	–	600	1.89	Kyriakou et al.[24]
Fe	0.28	600	17	Okazaki et al.[25]
Fe-BZY20	0.28	600	14	Okazaki et al.[25]
BZFY	0.28	600	3.4	Okazaki et al.[25]
Fe	1	550	14	Li et al.[26]
Fe-BCY	1	600	0.42	Li et al.[26]
W-Fe-BCY	1	550	0.57	Li et al.[26]
CeFe11	0.28	600	12	Okazaki et al.[27]
CeFe61	0.28	600	11	Okazaki et al.[27]
K,Al-Fe-BCY	0.39	650	0.67	Kosaka et al.[28]
LCuF	0.28	650	5.12	Guo et al.[29]
LF	0.28	650	1.78	Guo et al.[29]
Fe	0.79	600	7.2	Okazaki et al.[30]
Fe	–	550	3.8	Li et al.[10]
Fe in BCZY721 backbone	12.57	500	30.3	**This work**

Only peak ammonia formation rates r_{NH_3} reached are displayed. BCY, $BaCe_{0.9}Y_{0.1}O_{3-\delta}$; BCZYZ, $BaCe_{0.5}Zr_{0.3}Y_{0.16}Zn_{0.04}O_{3-\delta}$; LSTR40, $La_{0.5}Sr_{0.5}Ti_{0.6}Ru_{0.4}O_3$; BCYR, $BaCe_{0.8}Y_{0.1}Ru_{0.1}O_{2.9}$; PBSCF, $PrBa_{0.5}Sr_{0.5}Co_{1.5}Fe_{0.5}O_{5+\delta}$; BZCYYb1711, $BaCe_{0.1}Zr_{0.7}Y_{0.1}Yb_{0.1}O_{3-\delta}$; LDC, $La_{0.25}Ce_{0.75}O_{1.875}$; BCZY721, $BaCe_{0.7}Zr_{0.2}Y_{0.1}O_{3-\delta}$; LWO, $La_{5.5}WO_{11.25-\delta}$; BSTR, $Ba_{0.5}Sr_{0.5}Ti_{0.9}Ru_{0.1}O_{3-\delta}$; LST, $La_{0.3}Sr_{0.6}TiO_3$; I, impregnated; BCZG, $BaCe_{0.7}Zr_{0.1}Gd_{0.2}O_{3-\delta}$; BZY20, $BaZr_{0.8}Y_{0.2}O_{3-\delta}$; BZFY, $BaZr_{0.5}Fe_{0.4}Y_{0.1}O_3$; CeFe11, CeO_2-Fe_2O_3 1:1; CeFe61, CeO_2-Fe_2O_3 6:1; LCuF, $LaCu_{0.1}Fe_{0.9}O_{3-\delta}$; LF, $LaFeO_3$.

475°C, and 450°C, under OCV conditions as well as applied potentials of −1 and −1.4 V. Temperatures below 450°C were not investigated for the Fe-based electrode because the NH_3 formation rates under OCV conditions approached the detection limit of the ion-selective electrode (ISE), while the rates under polarization remained below 10^{-8} mol cm^{-2} s^{-1}.

After reduction, the catalyst loading of Fe was 1.35 mg_{Fe} cm^{-2}. Figures 3A–3C illustrate the NH_3 formation rates r_{NH_3} at all investigated cell voltages for the three temperatures, plotted as a function of the supplied cathode volume flow. The associated rate enhancement factors ρ, defined as the ratio of r_{NH_3} under polarization to r_{NH_3} at OCV, can be found in Figure S1. In addition, Figures 3D–3F present the corresponding current densities j at −1 and −1.4 V for 500°C, 475°C, and 450°C as a function of the supplied volume flow. The corresponding apparent electrochemical Faraday efficiencies FE_{NH_3} are shown on the secondary y axis. Here, FE_{NH_3} is used as a formal current-based comparison metric. It represents the fraction of the total current density j associated with NH_3 formation after subtraction of the thermocatalytic contribution determined at OCV. Contributions from the HER are not considered in this evaluation, and the quantity is not intended to imply proof of a direct faradaic N_2 reduction pathway. The detailed calculation is provided under "electrochemical characterization."

Peak r_{NH_3} were determined at −1.4 V and a flow rate of 60 NL h^{-1} for each temperature, yielding values of 2.91 × 10^{-8} mol cm^{-2} s^{-1} (78 mmol g_{Fe}^{-1} h^{-1}), 2.07 × 10^{-8} mol cm^{-2} s^{-1} (55 mmol g_{Fe}^{-1} h^{-1}), and 0.97 × 10^{-8} mol cm^{-2} s^{-1} (26 mmol g_{Fe}^{-1} h^{-1}) at 500°C, 475°C, and 450°C, respectively.

For comparison, a commercial Fe catalyst (KM1) tested in a laboratory fixed-bed reactor at 10 bar, 400°C, and an H_2:N_2 ratio of 3:1 achieved a formation rate of 26.5 mmol g_{Fe}^{-1} h^{-1}.[33] In their review, Humphreys et al. compared several reported Fe-based catalysts operated under different conditions in thermocatalytic fixed-bed experiments, including elevated pressures, and reported peak r_{NH_3} of approximately 30 mmol g_{Fe}^{-1} h^{-1}.[34–36] While a direct comparison between thermocatalytic fixed-bed data and electrocatalytically obtained NH_3 synthesis rates is inherently challenging due to the fundamentally different operating principles and reactor environments, gram-normalized performance metrics for electrochemical systems are scarcely reported in the literature. In this study, the weight of the whole cell is not taken into account in this context, only the catalyst introduced at the cathode itself. The comparison presented here should therefore be viewed primarily as an indication that exceptionally high mass-specific NH_3 synthesis rates can be achieved under electrochemical operation. These findings highlight the potential of electrochemical promotion to achieve high mass-specific NH_3 formation rates under atmospheric-pressure conditions.

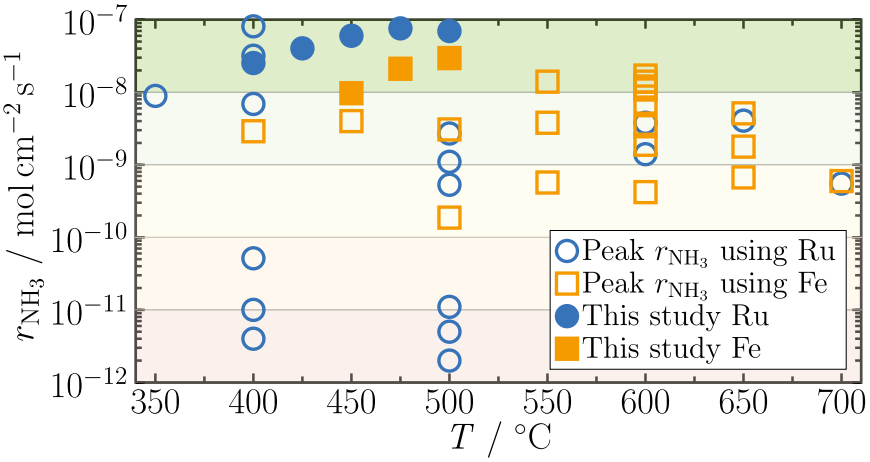

Figure 1. The peak NH_3 formation rates r_{NH_3} reported in the literature, as summarized in Table 1 and plotted as a function of temperature

Only the highest reported formation rate for each distinct electrode design at its respective operating temperature is displayed. The solid markers correspond to the results obtained in the present study.

The highest ρ were 244 (500°C, 40 NL h^{-1}), 273 (475°C, 50 NL h^{-1}), and 283 (450°C, 60 NL h^{-1}), each measured at −1.4 V. The noticeable dips in ρ can be attributed to deviating measurements under OCV conditions. These OCV data points deviate slightly from the overall trend, which leads to apparent dips in ρ despite only minor differences in the underlying r_{NH_3}.

The results clearly demonstrate that r_{NH_3} is positively influenced by temperature, applied cell voltage, and the volumetric flow rate supplied to the cathode. Across the entire temperature range studied, higher voltages and flow rates consistently lead to increased r_{NH_3}, highlighting the catalyst's high performance. Consequently, the highest formation rates are observed at −1.4 V in combination with high volumetric flows. A temperature-dependent trend is also apparent: r_{NH_3} decreases both at OCV and under polarization as the temperature is lowered.

At 500°C, increasing the cell voltage from −1.0 to −1.4 V results in only marginal improvements in r_{NH_3}. The measured rates remain close to one another and just below the equilibrium line, indicating that thermodynamic constraints may limit further NH_3 formation.

At 475°C, the equilibrium line shifts slightly toward higher values. However, r_{NH_3} does not increase relative to the rates observed at 500°C, suggesting that thermodynamics is not the primary limiting factor under these conditions. In this regime, decreasing the cell voltage has a more pronounced effect on r_{NH_3}, particularly at higher volumetric flow rates.

At 450°C, lowering the cell voltage from −1 to 1.4 V produces the largest relative increase in r_{NH_3}, as also reflected in the pronounced difference in ρ between these voltages. However, the rates remain far from the equilibrium line, indicating that kinetic limitations become increasingly dominant.

The average increase in r_{NH_3} between 450°C and 475°C at −1.4 V, across the investigated volume-flow range of 20 to 60 NL h^{-1}, amounts to a factor of approximately 2.2–2.4. This pronounced enhancement highlights the strong temperature dependence of the reaction rate under kinetically controlled conditions. In contrast, between 475°C and 500°C, the corresponding increase is limited to a factor of 1.4–1.5, indicating that the system gradually approaches thermodynamic constraints, thereby reducing the sensitivity of the formation rate to further temperature increments.

Peak FE_{NH_3} were determined at the highest flow rate of 60 NL h^{-1} for each temperature, yielding values of 11.88% (j = 63 mA cm^{-2}, −1 V), 6.76% (j = 90 mA cm^{-2}, −1.4 V), and 3.36% (j = 83 mA cm^{-2}, −1.4 V) at 500°C, 475°C, and 450°C, respectively. These values are among the upper range reported under similar conditions, as NH_3 synthesis typically competes with hydrogen evolution, which limits FE_{NH_3} to below 10% in most studies.[37]

At all investigated temperatures, an increase in the cathode feed flow rate resulted in a decrease in j. This behavior may be attributed to the reduced residence time of reactants at the electrode surface and to mass-transport limitations arising from insufficient diffusion of N_2 and H_2 into the porous structure. In addition, changes in surface coverage and possible suppression of HER at higher flow rates may contribute to the observed trend. Potential local cooling effects caused by the elevated gas flow

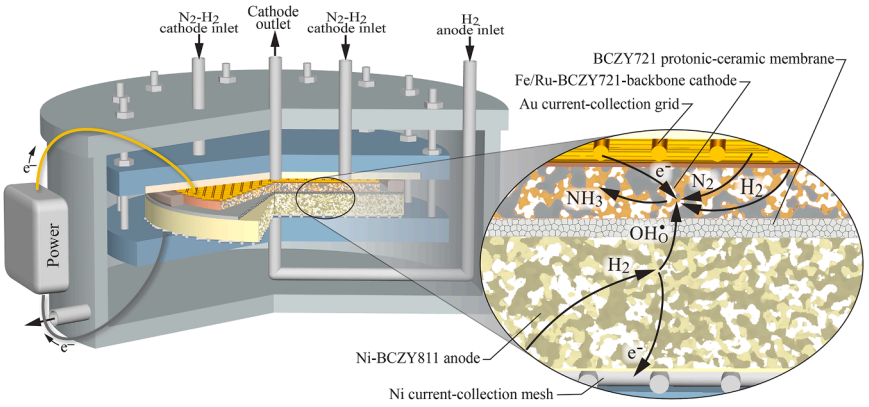

Figure 2. Schematic illustration of the double-flange setup, showing the cell mounted between the two flanges

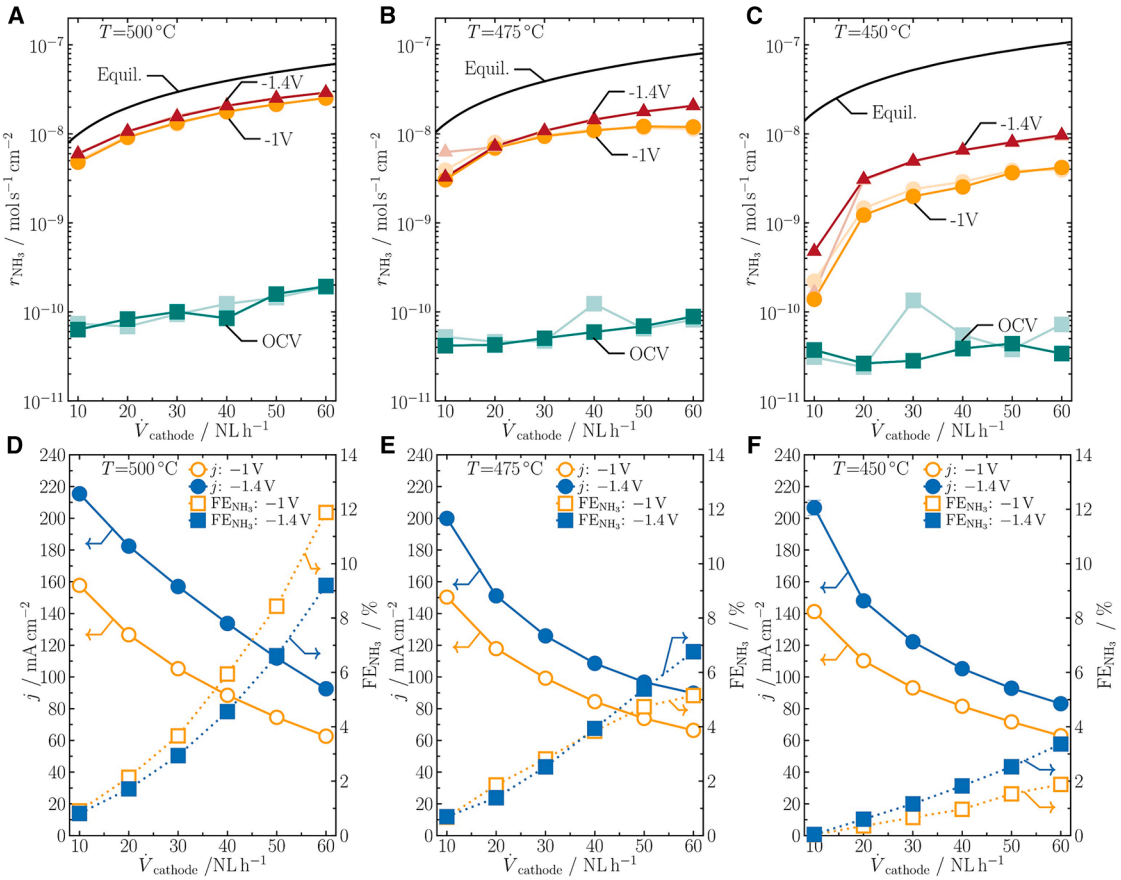

Figure 3. Flow-dependent performance of the PCC with an Fe-based cathode

(A–C) Ammonia formation rates r_{NH_3} for the Fe-based electrode plotted as a function of the supplied volume flow to the cathode at (A) 500°C, (B) 475°C, and (C) 450°C. The lighter symbols indicate the results of the second measurement at the same point. The thermodynamic equilibrium shown in each graph was calculated for a fixed H_2:N_2 ratio of 1:1 under OCV conditions, taking into account the active cell area, volume flow, and respective temperature.

(D–F) The corresponding current densities j and the apparent electrochemical Faraday efficiencies FE_{NH_3} are plotted as a function of the supplied volume flow to the cathode at (D) 500°C, (E) 475°C, and (F) 450°C. The j values were recorded during the NH_3 sampling period after stabilization of the respective operating condition.

may also contribute, although these were not detected by the thermocouples positioned near the cell. No significant effect on the current density was observed when the anode volume flow was varied in separate experiments.

At 500°C, the higher FE_{NH_3} values were consistently observed at −1 V. At 475°C, the FE_{NH_3} at −1 and −1.4 V were close to each other. In contrast, at 450°C, highest FE_{NH_3} occurred at −1.4 V. These findings confirm that at 500°C, r_{NH_3} is primarily constrained by thermodynamics, with higher absolute voltages offering little benefit due to equilibrium limitations. As the temperature decreases, the equilibrium shifts toward higher NH_3 yields. However, the process becomes increasingly kinetically controlled, making the system more responsive to voltage-driven promotion.

Ru electrode

For the cell employing a pure Ru electrode, measurements were conducted at five temperatures, 500°C, 475°C, 450°C, 425°C, and 400°C, under OCV conditions as well as applied potentials of −1 and −1.4 V. After reduction, the Ru catalyst loading was 1.34 mg_{Ru} cm^{-2}, which corresponds to nearly the same amount of catalyst as that of the Fe electrode. Figures 4A–4E show the r_{NH_3} for all temperatures and voltage levels as a function of the supplied gas volume. The corresponding ρ are displayed in Figure S2. Figures 4F–4J show the corresponding current density j at −1 and −1.4 V for 500°C, 475°C, 450°C, 425°C, and 400°C as a function of the supplied volume flow. The associated FE_{NH_3} are displayed on the secondary y axis.

Peak r_{NH_3} were determined at −1.4 V and a flow rate of 60 NL h^{-1} for each temperature, yielding values of 3.54 × 10^{-8} mol cm^{-2} s^{-1} (95 mmol g_{Ru}^{-1} h^{-1}), 2.57 × 10^{-8} mol cm^{-2} s^{-1} (69 mmol g_{Ru}^{-1} h^{-1}), 1.57 × 10^{-8} mol cm^{-2} s^{-1} (42 mmol g_{Ru}^{-1} h^{-1}), 0.74 × 10^{-8} mol cm^{-2} s^{-1} (20 mmol g_{Ru}^{-1} h^{-1}), and 0.24 × 10^{-8} mol cm^{-2} s^{-1} (6 mmol g_{Ru}^{-1} h^{-1}) at 500°C, 475°C, 450°C, 425°C, and 400°C, respectively. As a point of reference, Humphreys et al. and Fang et al. reviewed a range of Ru-based catalysts tested under thermocatalytic fixed-bed conditions at elevated pressures, reporting maximum r_{NH_3} of approximately 300 mmol g_{Ru}^{-1} h^{-1} (10 MPa and 400°C).[34,38–41]

The rate enhancement factors ρ for the PCC with the Ru electrode remain relatively low, ranging from 1.13 to 2.10 across all temperatures and polarization conditions, with the highest values consistently observed at the lowest volumetric flow rates. The maximum ρ was observed at 425°C and 10 NL h^{-1}, with a value of 2.10. The comparatively modest enhancement of the Ru-based electrode shows that its NH_3 formation rate responds less strongly to polarization than that of the Fe-based electrode under the investigated conditions. The enhancement factor ρ increases gradually with decreasing temperature, although the effect is marginal and non-uniform, suggesting that thermodynamic limitations at higher temperatures may restrict further increases in the formation rate (see Figures S3A and S3B). At 400°C, however, a downturn is observed, indicating a diminished response to polarization.

Starting from 400°C, r_{NH_3} at −1.4 V increases by a factor of approximately 3.2 upon heating to 425°C. Further increasing the temperature to 450°C results in a rate enhancement of a factor of about 2.1 relative to 425°C, while at 475°C and 500°C, the corresponding factors decrease to roughly 1.6 and 1.2, respectively. This corresponds to a decreasing apparent activation energy with increasing temperature, consistent with the observed curvature of the Arrhenius plots (see Figure S4). While surface saturation or diffusion limitations cannot be entirely ruled out, the trend is most likely dominated by thermodynamic constraints at elevated temperatures, which suppress further rate increases despite higher thermal energy.

Similar to the Fe-based electrode, an increase in the cathode feed flow rate resulted in a decrease in j at all investigated temperatures. Peak FE_{NH_3} values were determined at each temperature for an applied voltage of −1.4 V, occurring at the highest flow rate of 60 NL h^{-1}, with a maximum FE_{NH_3} of 10.86%, achieved at a j of 23 mA cm^{-2} and a temperature of 475°C. At all investigated temperatures and under most operating conditions, increasing the magnitude of the applied cell voltage increases the apparent FE_{NH_3}, with the largest enhancement observed at 475°C and high cathode flow rates, demonstrating a positive response to polarization.

However, at 500°C and at 425°C and below, increasing the cell voltage yields only a marginal improvement in FE_{NH_3}, likely due to thermodynamic and kinetic limitations, respectively. Moreover, although ρ increases slightly as the temperature decreases to 425°C, the accompanying reduction in current density shows that the measured r_{NH_3} does not scale directly with the total current density. Our previous work similarly showed comparatively low r_{NH_3} in a configuration relying primarily on transported protonic species, whereas increasing the H_2 partial pressure on the cathode side strongly enhanced NH_3 synthesis. These observations suggest that proton flux alone is insufficient to explain the measured performance. However, the present data do not distinguish among electric-field effects, current-related processes, changes in catalyst state or adsorbate coverage, and other interfacial contributions and therefore cannot provide a conclusive determination of the reason for this effect. The observed differences between Fe- and Ru-based electrodes are therefore discussed here in terms of catalyst-specific responses to polarization rather than as proof of a unique underlying mechanism.

Impedance measurements were conducted at all temperatures and, in each case, under the lowest gas-flow configuration. The Nyquist plots exhibit a markedly enlarged semicircular arc for the Ru-based electrode, indicating a substantially higher polarization resistance. This finding is consistent with the comparatively lower current densities observed for the Ru-based cell. As the cell configuration and electrolyte thickness are comparable to those of the Fe-based cell, the lower current density is reasonably attributed to increased electrode-related polarization losses, most likely associated with slower charge-transfer kinetics and/or interfacial limitations at the electrode-electrolyte interface under the investigated conditions. Possible contributions from catalyst-specific HER behavior cannot be excluded but were not separately resolved in the present study. The corresponding impedance data are provided in Figures S5 and S6. Equivalent-circuit fitting (Figure S7) of selected impedance spectra further supports this interpretation. The fitted parameters, summarized in Table S3, indicate larger polarization-related resistive contributions for the Ru-based cell than for the Fe-based cell.

Comparison of Fe vs. Ru electrode

Figure 5 summarizes the peak r_{NH_3} values for the Fe- and Ru-based electrodes measured at each temperature. Since the highest rates were consistently observed at a flow rate of 60 NL h^{-1}, only these values are displayed. In addition, measurements were performed at an even higher cathode flow rate of 100 NL h^{-1} to examine whether this trend continues.

A superior catalytic activity of Ru toward NH_3 formation compared with the Fe-based electrode is clearly evident from the catalyst-specific formation rates. Under identical conditions of −1.4 V and 60 NL h^{-1}, the Ru-based electrode exhibited 18%, 23%, and 58% higher r_{NH_3} than the Fe-based counterpart at 500°C, 475°C, and 450°C, respectively. At a high cathode flow rate of 100 NL h^{-1}, this trend is further accentuated, reflecting the inherently faster reaction kinetics of Ru compared with Fe.

A comparison of ρ shows that the Fe-based electrode exhibits values more than two orders of magnitude higher than those of the Ru electrode. However, the comparatively low ρ observed for Ru cannot be explained solely by its high baseline activity, as the measured r_{NH_3} values remain well below the equilibrium limit at temperatures below 500°C. Instead, the results show that the Ru-based electrode is less responsive to polarization than the Fe-based electrode under the investigated conditions.

When the volume flow was increased to 100 NL h^{-1}, the Fe electrode produced slightly more NH_3 only at 500°C, whereas at decreasing temperatures, the rates were lower than those measured at 60 NL h^{-1}. This behavior may be attributed to changes in gas-solid interaction dynamics at higher flow rates, where the reduced residence time and altered boundary layer conditions can affect the local reactant concentrations and surface coverage. At 500°C, faster kinetics likely compensate for these effects, leading to slightly higher rates.

In contrast, for the Ru-based electrode, r_{NH_3} increases at 100 NL h^{-1} across the entire temperature range, indicating intrinsically fast reaction kinetics that are largely independent of residence time or mass transport limitations, even at lower temperatures.

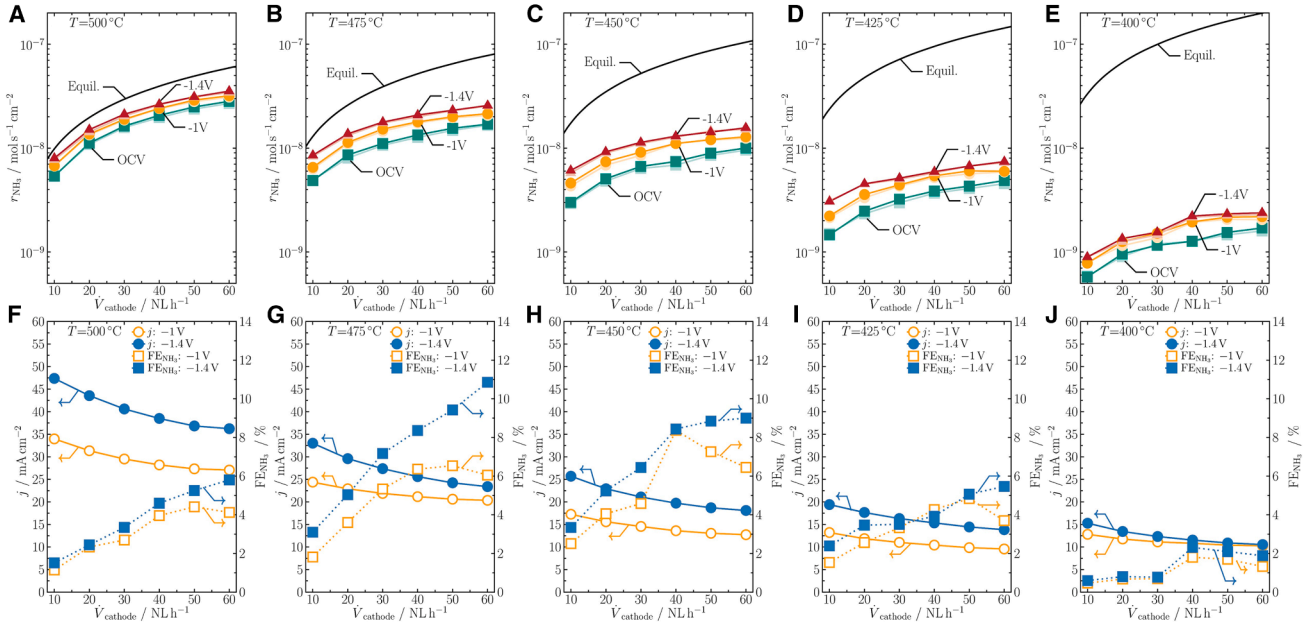

Figure 4. Flow-dependent performance of the PCC with an Ru-based cathode

(A–E) Ammonia formation rates r_{NH_3} for the Ru-based electrode as a function of the supplied cathode volume flow at (A) 500°C, (B) 475°C, (C) 450°C, (D) 425°C, and (E) 400°C. The lighter symbols indicate the results of the second measurement at the same point. The thermodynamic equilibrium shown in each graph was calculated for a fixed H_2:N_2 ratio of 1:1 under OCV conditions, taking into account the active cell area, volume flow, and respective temperature.

(F–J) The corresponding current densities *j* and the apparent electrochemical Faraday efficiencies FE_{NH_3} are plotted as a function of the supplied volume flow to the cathode at (F) 500°C, (G) 475°C, (H) 450°C, (I) 425°C, and (J) 400°C. The *j* values were recorded during the NH_3 sampling period after stabilization of the respective operating condition.

Figure 6 shows a comparison of r_{NH_3} for the Fe- and Ru-based electrodes at 60 NL h^{-1} and a polarization of −1.4 V, separating the respective contributions of thermocatalytic and electrocatalytic NH_3 formation. For Fe, the majority of the measured rate at −1.4 V corresponds to the polarization-associated increase, whereas for Ru, the OCV contribution remains dominant.

Under polarization, Fe achieves r_{NH_3} values comparable to those of Ru, showing that Fe responds substantially more strongly to the applied cell voltage, whereas the additional response of Ru remains limited under the investigated conditions.

Figure 7 shows cross-sectional scanning electron microscopy (SEM) images of the cell with the Fe-containing electrode (left) and the Ru electrode (right).

Both images demonstrate good adhesion of the respective catalyst to the underlying scaffold layer, with the catalysts well integrated into the porous backbone and forming a strong interfacial connection. Additional energy dispersive X-ray spectroscopy (EDX) mapping results supporting this observation are provided in Figure S8. For both cells, the electrolyte has a thickness of approximately 26 μm. This comparatively thick electrolyte was intentionally used to suppress excessively high *j* at the applied

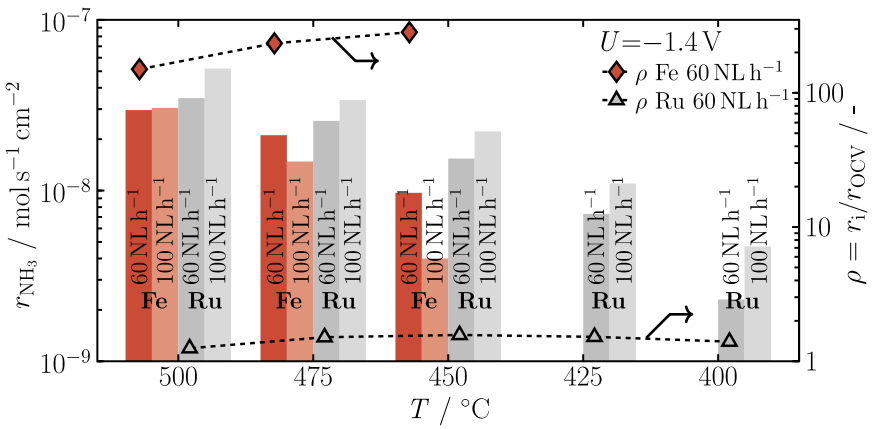

Figure 5. Comparison of peak r_{NH_3} between Fe and Ru electrodes with a catalyst loading of 1.35 mg_{Fe} cm^{-2} and 1.34 mg_{Ru} cm^{-2}, respectively

All values were measured at an applied cell voltage of −1.4 V. The enhancement factors ρ for 60 NL h^{-1} are also included.

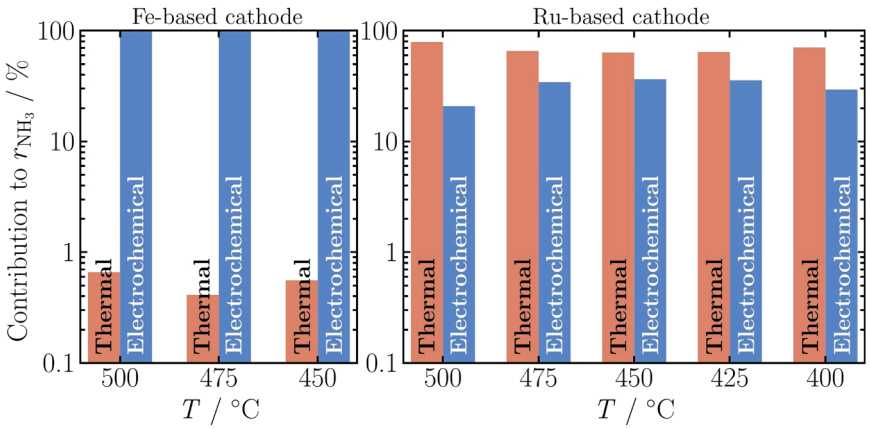

Figure 6. Thermocatalytic vs. electrocatalytic contributions to NH_3 formation on Fe- and Ru-based electrodes

Values are taken from Figure 5 at 60 NL h^{-1}.

cell voltages. This was motivated by previous experiments showing that NH_3 formation depended primarily on the applied voltage rather than on j,[9] in agreement with literature reports.[26] In addition, two type-K thermocouples positioned close to the cell showed no temperature change greater than 1 K during operation, indicating negligible Joule-heating effects under the investigated conditions. The Ru electrode shows a finer catalyst morphology than the Fe electrode. This observation is supported by a quantitative image analysis (n = 50), which yielded average particle diameters of 224 ± 58 nm for Fe and 176 ± 52 nm for Ru.

Ru catalyst loading

In an additional experiment, the Ru catalyst loading was increased to nearly twice the previous value, reaching 2.61 mg_{Ru} cm^{-2}, to evaluate its influence on NH_3 synthesis. The overall cell behavior and performance trends were comparable to those obtained with a loading of 1.34 mg_{Ru} cm^{-2}; therefore, only the peak r_{NH_3}, measured at 60 NL h^{-1} and −1.4 V, are presented in Figure 8. Here, additional measurements were also conducted at the same voltage and 100 NL h^{-1}. For reference, the peak values from the previous cell are included for comparison.

A higher Ru catalyst loading leads to a significantly increased r_{NH_3}. At 500°C and 475°C, the rates approach the thermodynamic equilibrium, reaching peak values at 475°C of 7.70×10^{-8} mol cm^{-2} s^{-1} (106 mmol g_{Ru}^{-1} h^{-1}) at 100 NL h^{-1} and 5.93×10^{-8} mol cm^{-2} s^{-1} (FE_{NH_3} = 20.34%) at 60 NL h^{-1}. For the cell with the higher Ru loading, a pronounced inflection is observed at 475°C, indicative of thermodynamic limitations on NH_3 formation, which is further reflected in the Arrhenius plots (Figure S9) as a clear downturn at high temperatures. This feature is absent in the cell with lower Ru loading, where r_{NH_3} remain well below the thermodynamic limit.

Although the equilibrium NH_3 production rate declines exponentially with increasing temperature, favoring low-temperature operation, kinetic constraints at these temperatures substantially limit the achievable production rates.

The ρ factors for the cell with higher catalyst loading remain within a similar range, with values of 1.66 at 400°C and decreasing to 1.04 at 500°C, showing that the response to polarization becomes increasingly small as the measured r_{NH_3} approaches equilibrium conditions.

For both electrodes, increasing the total gas flow to 100 NL h^{-1} further enhances r_{NH_3}, confirming that the Ru catalyst provides sufficiently fast reaction kinetics. The r_{NH_3} values at 100 NL h^{-1} of the nearly doubled Ru loading surpass those of the lower loading by factors of approximately 1.3, 2.2, 2.7, 3.7, and 5.4 at 500°C, 475°C, 450°C, 425°C, and 400°C, respectively. This more-than-proportional increase in r_{NH_3} with decreasing temperature may be attributed to the additional Ru sites contributing more effectively under kinetically controlled conditions, where the overall reaction rate is directly sensitive to the number of available active sites. At higher temperatures, the reaction approaches diffusion or equilibrium limitations, leading to a less pronounced enhancement upon increased catalyst loading.

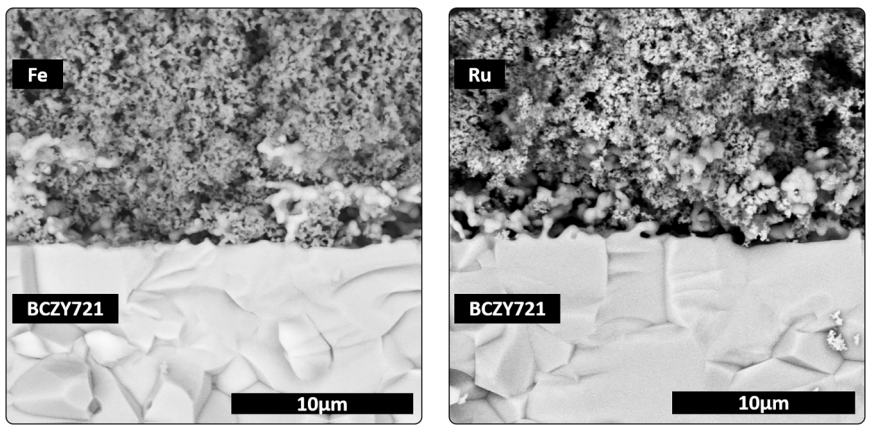

Figure 7. Cross-sectional SEM images acquired in backscattered electron mode of the Fe-based electrode (left) and the Ru-based electrode (right)

The bright bottom layer corresponds to the BCZY721 electrolyte. Above the electrolyte, the porous BCZY721 backbone is visible, appearing bright in backscattered electron (BSE) contrast. The respective catalyst is distributed both on the surface and partially within the porous structure of the backbone. The scale bars represent 10 µm each.

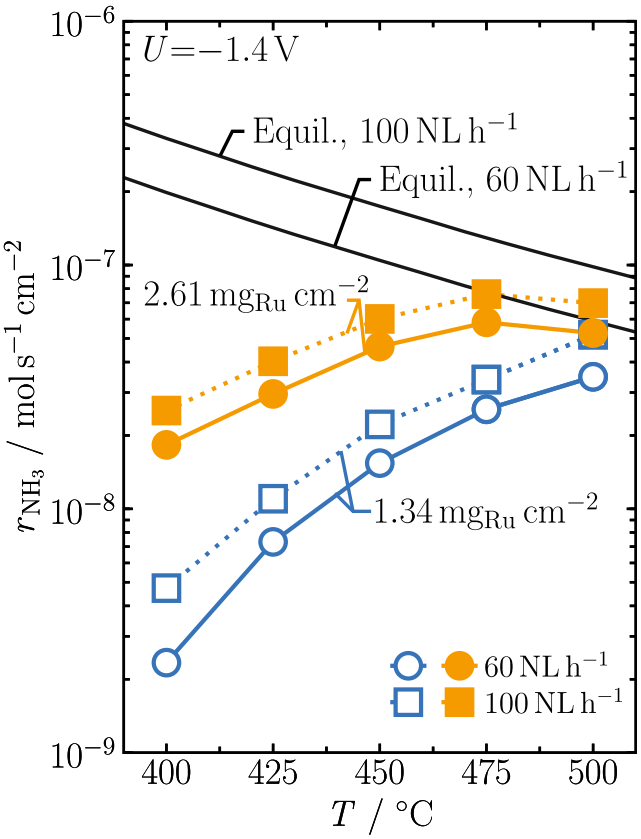

Figure 8. Comparison of ammonia formation rates r_{NH_3} for electrodes containing 1.34 and 2.61 mg$_{Ru}$ cm^{-2}

The thermodynamic equilibrium was calculated for a fixed H_2:N_2 feed ratio of 1:1 under OCV conditions at total flow rates of 60 and 100 NL h^{-1}. All r_{NH_3} were measured at an applied voltage of −1.4 V.

DISCUSSION

The comparative investigation of Fe- and Ru-based electrodes with nearly identical catalyst loadings revealed pronounced differences in their NH_3 synthesis performance and response to polarization on proton-conducting BCZY721 membranes. Under OCV conditions, the Ru-based electrode exhibited substantially higher intrinsic catalytic activity than the Fe-based electrode, with NH_3 formation rates approximately two orders of magnitude higher. In contrast, the Fe-based electrode showed a markedly stronger relative response to polarization, reaching enhancement factors of up to ρ = 283 at 450°C and approaching the NH_3 formation rates of the Ru-based electrode under applied cell voltage. The Ru-based electrode exhibited only a limited additional rate increase under comparable conditions, with $\rho < 3$.

These results demonstrate that intrinsic catalytic activity and response to polarization represent distinct catalyst-dependent performance characteristics. Ru provides high baseline NH_3 synthesis activity over the investigated temperature range, whereas Fe exhibits a substantially larger rate modulation under polarization. The different behavior of the two electrodes cannot be explained by intrinsic thermocatalytic activity alone and indicates that catalyst identity strongly influences the response of the electrode to the applied cell voltage.

The fabrication approach developed for the Ru-based electrode, combining reduction and *in situ* sintering, produced a porous and mechanically adherent catalyst layer suitable for operation on the enlarged cell geometry. Together with the Fe-based electrode architecture, this demonstrates that both catalyst systems can be integrated into a porous BCZY721 backbone over an active area of 12.57 cm^2.

Overall, the results show that catalyst selection for electrochemically assisted NH_3 synthesis should consider both intrinsic catalytic activity and the magnitude of the response to polarization. Ru is advantageous with respect to baseline activity, while Fe exhibits a considerably stronger relative rate enhancement under applied cell voltage. Electrode concepts combining complementary catalyst properties may therefore be of interest for future development, although their performance and underlying interactions require dedicated investigation.

Limitations of the study

The present study was designed as a comparative performance investigation of Fe- and Ru-based cathodes using closely comparable cell configurations and systematically varied operating conditions. It was not designed to provide a definitive mechanistic assignment of the observed catalyst-specific responses to polarization. Accordingly, the measurements quantify differences in NH_3 formation rate, current density, impedance response, and relative rate enhancement but do not independently resolve the contributions of electric field, electric current, proton transport, catalyst-state changes, or other interfacial effects.

Previous studies have proposed that protonic species and surface proton transfer may contribute to NH_3 formation under polarized conditions through alternative hydrogenation or N_2 activation pathways. However, the relevance of such mechanisms for the Fe- and Ru-based electrodes investigated here cannot be established from the present data.[42,43]

An experimental limitation concerns the complete exclusion of trace NH_3 contamination. Fresh trapping solution was routinely analyzed as a blank, and the ion-selective-electrode method was cross-validated against UV-visible analysis. In addition, the very low NH_3 formation rates measured for the Fe-based electrode under OCV conditions, which approached the ISE detection limit at temperatures below 450°C, indicate that any constant background contribution was negligible relative to the rates observed under polarization. The systematic dependence of the measured NH_3 formation rates on temperature, applied cell voltage, and gas flow further argues against trace contamination as the dominant origin of the reported trends. Nevertheless, the controls performed in this study do not provide the same level of source verification as system-specific blank electrolysis under pure N_2 or isotope-labeling experiments. Future work should therefore include blank measurements under pure N_2 at OCV and under polarization, together with $^{15}N_2$ isotope labeling, to provide an unequivocal assignment of the nitrogen source.

Dedicated transient experiments are also required to determine whether the enhanced NH_3 formation under polarization represents an immediately reversible response or is influenced by slower changes in the catalyst state. Measurements involving

repeated switching of the applied voltage on and off, followed by NH_3 quantification after returning to OCV, could distinguish reversible polarization effects from persistent activation, reduction, restructuring, or removal of surface species. Such experiments should be performed at different gas flow rates and with sufficient temporal resolution to account for gas residence time and the response time of the analytical system.

Cyclic voltammetry and measurements over a broader range of applied cell voltages could provide additional information on potential-dependent changes in the electrochemical response of the Fe- and Ru-based electrodes. Complementary *operando* or quasi-*operando* characterization would be required to assess whether polarization-induced changes in the catalyst state contribute to their different behaviors. Hydrogen-isotope experiments could further clarify the role of cathode-side hydrogen in the observed NH_3 formation.

Finally, a dedicated experimental design would be required to distinguish the respective contributions of electric field, electric current, proton transport, and the proton-conducting membrane. Relevant control configurations could include electronically polarized catalyst systems without a proton-conducting membrane and cells in which proton transport is selectively suppressed. Such experiments would help determine whether the observed rate enhancement is primarily associated with polarization of the catalyst surface, ionic transport through the electrolyte, or other interfacial processes.

The measurements reported in the present study represent stabilized operating points after a defined stabilization period, but they do not constitute dedicated long-term durability tests. Extended operation under selected constant conditions would therefore be required to determine whether the observed performance and response to polarization are maintained over longer time periods.

These investigations would enable a more robust interpretation of the different responses of Fe and Ru. Until such data are available, the present results should be understood as a quantitative comparison of catalyst performance and response to polarization rather than as proof of a unique electrochemical or surface-reaction mechanism.

METHODS

Powders

Each material used in this study is commercially available. The anode and electrolyte layers were fabricated using the following materials: the anode was made of $BaCe_{0.8}Zr_{0.1}Y_{0.1}O_{3-\delta}$ (BCZY811) (CerPoTech AS) and NiO (JT Baker), while the electrolyte consisted of $BaCe_{0.7}Zr_{0.2}Y_{0.1}O_{3-\delta}$ (BCZY721) (CerPoTech AS) and ZnO (Sigma Aldrich). The cathode was prepared using BCZY721 (CerPoTech AS) with Ru(IV)oxide (99.95% metal basis, Premion) or α-Fe_2O_3 (<5 μm, 96%, Merck). As a pore former, TIMREX SFG75 graphite (TIMCAL) was used.

Cell fabrication

Anode

The anode support was fabricated by tape casting using a slurry consisting of NiO and BCZY811 in a weight ratio of 1.5:1, graphite as a pore former, Nuosperse as a dispersant, and a solvent mixture of butanone and ethanol. The slurry was homogenized for 22 h using a Turbula T2F mixer (WAB). Subsequently, polyvinyl butyral (binder) and PEG/TEG-EH (plasticizers, Eastman) were added, and the mixture was milled for an additional 3 h. After resting for 22 h, the slurry was degassed under vacuum for 10 min. It was then tape casted onto a glass plate covered with a polymer sheet using a ZAA 2300 film applicator (Zehntner GmbH) and dried at room temperature for 24 h. The resulting green tapes had a thickness of approximately 750 μm and a surface area of about 700 cm^2. Circular samples with a diameter of 77 mm (46.57 cm^2) were subsequently cut for further processing.

Electrolyte

BCZY721 was mixed with a carrier formulation composed of α-terpineol and ethyl cellulose, along with 0.5 wt % ZnO as a sintering aid. The mixture was initially ground using an automatic mortar (Retsch RM200) for 20 min, followed by further homogenization in a roller mill. The resulting electrolyte ink was applied onto the green anode tape cutouts via screen printing using an EKRA E2 screen printer. To achieve increased electrolyte thicknesses, multiple screen-printing cycles were carried out with intermediate drying steps. The half-cells were then co-sintered at 1,400°C for 8 h, incorporating intermediate dwell stages at 250°C for solvent removal and 550°C for burnout of the graphite pore former in the anode support.

Cathode

The cathode was applied via two-step screen printing. Initially, a porous BCZY721 backbone (BCZY721:graphite, 1.5:1) was prepared by dispersing it in a carrier mixture consisting of α-terpineol and ethyl cellulose, achieving a solid content of 45 wt %. This mixture was subsequently printed onto the sintered half-cell, allowed to dry in air until a matte finish was attained, and then sintered at 1,350°C for a duration of 1 h. The heating and cooling ramps were controlled at a rate of 3 K min^{-1}. The resulting porous structure served as a scaffold for catalyst deposition.

Subsequently, a low-viscosity catalyst ink (catalyst oxide powder and the same carrier mixture) was "screen-pressed," i.e., applied via screen printing into the porous scaffold in order to infiltrate the pre-sintered backbone. Further methodological details on the screen-pressing approach used for catalyst incorporation can be found in our previous work.[44] Two different catalyst inks were formulated, each designed to achieve optimal distribution within the backbone structure:

(1) Fe electrode: consisting of pure Fe_2O_3 with a solid loading of 45 wt %, sintered in air at 850°C for 1 h with heating and cooling ramps of 3 K min^{-1};
(2) Ru electrode: composed of pure RuO_2 with a solid loading of 60 wt %, dried in air at 100°C for 1 h.

The final cells had a diameter of 52 mm (21.24 cm^2 total area) and an active cathode area of 12.57 cm^2 (40-mm diameter). The final appearance of the cells employing Fe and Ru electrodes is presented in Figure 9. The underlying backbone layer is entirely covered by the catalyst inks and, consequently, is not visible.

Electrochemical characterization

For testing and electrochemical characterization, the PCCs were mounted in a specifically modified, ceramic-lined double-flange

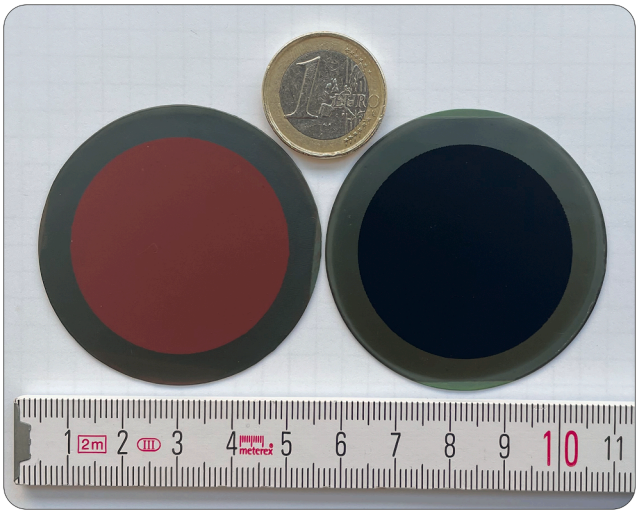

Figure 9. Final design of the cells equipped with Fe-based (left) and Ru-based (right) electrodes

dual chamber test rig (Fiaxell SOFC Technologies). Figure 2 provides a schematic overview of the test bench, including a magnified cross section of the cell and the configuration of the electrical contacts. The cathode was contacted using a gold grid, whereas nickel foam was employed for the anode contact.

The sealing, heating, and reduction procedures of the Fe electrode have been described previously.[44] The Ru electrode, after drying in air at 100°C, was sintered *in situ* under a reducing atmosphere (10% H_2 in N_2), as RuO_2 can be fully reduced by H_2 at temperatures as low as 100°C.[45] The temperature was then raised to 500°C at a rate of 1 K min^{-1} and maintained for 3 h, while the H_2 concentration was gradually increased to 50%. Sintering of the RuO_2 ink in air following the same procedure as for the Fe_2O_3 ink caused significant catalyst agglomeration at temperatures of 700°C and above, while sintering at lower temperatures resulted in poor adhesion to the substrate. Corresponding SEM images of these samples are presented in the supplemental information (see Figure S10). Samples sintered in air below 600°C are not shown, since the Ru layer was entirely detached from the electrolyte during processing. Therefore, an *in situ* approach was trialed and resulted in the desired characteristics.

The SEM images were acquired using an FEI Quanta 200 F at an acceleration voltage of 15 kV.

Electrochemical impedance spectroscopy (EIS) measurements were performed using a Zahner Zennium instrument (Zahner) over a frequency range of 100 mHz to 100 kHz, with an AC amplitude of 15 mV at OCV. Additionally, impedance measurements were conducted using a Solartron SI 1255 HF frequency response analyzer coupled with a Solartron SI 1287 electrochemical interface over a frequency range of 1 MHz to 1 Hz.

Identical experimental protocols were employed for the characterization of all electrodes. An H_2/N_2 gas mixture of 1:1 was supplied to the cathode, while the anode feed was kept constant throughout all experiments at 6 NL h^{-1} of H_2 and 6 NL h^{-1} of N_2. On the anode side, N_2 was added solely to dilute the H_2 stream and to match the H_2 partial pressure to that on the cathode side. The 1:1 H_2/N_2 ratio on the cathode was selected because prior experiments had shown that a comparable Fe-based electrode exhibited optimal performance close to this composition.[9] The gas inlet to the cathode was dehumidified directly before the reactor inlet using a 3 Å molecular sieve, as previous tests employing Fe electrodes had shown that small amounts of water resulted in deactivation of the catalyst. Dry inlet conditions were therefore deliberately used throughout this study to ensure well-defined and directly comparable baseline conditions for both Fe- and Ru-based electrodes.

NH_3 formation was quantified under thermocatalytic conditions at OCV and during electrochemical polarization at 1 and 1.4 V by collecting the cathode exhaust gas in an NH_3 trapping solution and subsequently determining the trapped NH_3 concentration using a high-performance NH_3-ion-selective electrode (Orion, 9512HPBNWP, Thermo Scientific). The applied cell voltages of −1 and −1.4 V were selected on the basis of previous experiments and preliminary tests.[9]

The strongest increase in r_{NH_3} was consistently observed between OCV and −1 V, whereas the additional increase at −1.4 V was generally smaller. More negative voltages led to increasing instability of the Fe-based electrode and were therefore not considered further.

Measurements were conducted at seven different total flow rates to the cathode, ranging from 10 to 60 NL h^{-1}, as well as at 100 NL h^{-1}. At each operating condition, the system was allowed to stabilize for 10 min to reach steady-state conditions. Subsequently, two consecutive gas samples were collected from the cathode exhaust for 5 min each by bubbling the exhaust gas through 0.01 M H_2SO_4 to trap the formed NH_3. The cathode exhaust was not introduced into the trapping solution at reactor temperature but was first cooled to room temperature in the downstream gas line before entering the acidic trap. No significant loss of trapping solution was observed under the applied sampling conditions. Fresh trapping solution was routinely analyzed as a blank to identify possible background contamination. In addition, the ISE-based NH_3 quantification used in this work had previously been cross-validated against UV-visible analysis over a broad concentration range, with deviations below 10% (Figure S11).

The NH_3 formation rate, r_{NH_3}, is calculated according to the following expression:

$$r_{NH_3} = \frac{c_{NH_3} * N_{total} * k}{t * A * 10^6}.$$

Here, c_{NH_3} denotes the concentration of NH_3 in the trapping solution, N_{total} represents the total amount of substance, k is the correction factor of the calibrated ISE, t is the time in seconds, and A is the active surface area in square centimeters.

The rate enhancement factor, ρ, is determined by

$$\rho = \frac{r}{r_0} = \frac{r_0 + \Delta r}{r_0}$$

and represents the ratio of catalytic rates in the presence r and absence r_0 of polarization. Throughout this article, the reported

ρ values are determined from the mean of the experimentally measured r_{NH_3} values.

The apparent electrochemical Faraday efficiency, FE_{NH_3}, is calculated as follows:

$$FE_{NH_3} = \frac{n * F * \left(r_{NH_3,j} - r_{NH_3,OCV}\right)}{j} * 100.$$

It represents a formal current-based comparison metric for the fraction of the electric current density j associated with NH_3 formation at applied voltage, $r_{NH_3,j}$, after subtraction of the thermocatalytic contribution determined at OCV, $r_{NH_3,OCV}$. This quantity is not intended to imply proof of a direct faradaic N_2 reduction pathway. Here, n denotes the number of electrons transferred per molecule of product formed, and F is the Faraday constant.

RESOURCE AVAILABILITY

Lead contact

Requests for further information and resources should be directed to and will be fulfilled by the lead contact, Olaf Deutschmann (deutschmann@kit.edu).

Materials availability

No new materials were generated in this study. All materials used are described in the methods section, including manufacturer information.

Data and code availability

- The authors declare that the data supporting the findings of this study are available within the article and supplemental information.
- This paper does not report original code.
- All other items are available from the lead contact (deutschmann@kit.edu) upon request.

ACKNOWLEDGMENTS

We acknowledge omegadot software and consulting GmbH for providing the software tool DETCHEM. This project was funded by the Deutsche Forschungsgemeinschaft (DFG, German Research Foundation) (460038541) and by the National Science Foundation (NSF) (2140971) under the NSF-DFG Echem initiative (DE 659/14-1).

AUTHOR CONTRIBUTIONS

Conceptualization, P.B., R.J.K., J.D., and O.D.; methodology, P.B. and K.E.; investigation, K.E., P.B., and E.P.M.; writing – original draft, P.B.; writing – review and editing, E.P.M., D.S., R.J.K., J.D., and O.D.; funding acquisition, R.J.K. and O.D.; resources, J.D. and O.D.; supervision, J.D. and O.D.

DECLARATION OF INTERESTS

The authors declare no competing interests.

DECLARATION OF GENERATIVE AI AND AI-ASSISTED TECHNOLOGIES IN THE WRITING PROCESS

During the preparation of this work, the authors used ChatGPT (OpenAI) to improve the readability and linguistic clarity of the manuscript. The authors reviewed and edited the output as needed and take full responsibility for the content of the published article.

SUPPLEMENTAL INFORMATION

Supplemental information can be found online at https://doi.org/10.1016/j.xcrp.2026.103482.

Received: February 10, 2026
Revised: June 30, 2026
Accepted: July 14, 2026
Published: August 6, 2026

REFERENCES

1. IEA (2021). Ammonia Technology Roadmap (IEA). https://www.iea.org/reports/ammonia-technology-roadmap.
2. Liang, M., Kim, J., Xu, X., Sun, H., Song, Y., Jeon, S., Shin, T.H., Shao, Z., and Jung, W. (2025). Electricity-to-ammonia interconversion in protonic ceramic cells: advances, challenges and perspectives. Energy Environ. Sci. *18*, 3526–3552. https://doi.org/10.1039/D4EE06100D.
3. Vieri, H.M., Kim, M.-C., Badakhsh, A., and Choi, S.H. (2024). Electrochemical Synthesis of Ammonia via Nitrogen Reduction and Oxygen Evolution Reactions - A Comprehensive Review on Electrolyte-Supported Cells. Energies *17*, 441. https://doi.org/10.3390/en17020441.
4. Hu, Q., Tian, C., Bao, D., Zhong, H., and Zhang, X. (2024). Protonic ceramic electrochemical cells: Opportunities and challenges for ammonia synthesis. Next Energy *4*, 100144. https://doi.org/10.1016/j.nxener.2024.100144.
5. Saadatjou, N., Jafari, A., and Sahebdelfar, S. (2015). Ruthenium Nanocatalysts for Ammonia Synthesis: A Review. Chem. Eng. Commun. *202*, 420–448. https://doi.org/10.1080/00986445.2014.923995.
6. Nørskov, J.K. (1991). Electronic factors in catalysis. Prog. Surf. Sci. *38*, 103–144. https://doi.org/10.1016/0079-6816(91)90007-q.
7. Skúlason, E., Bligaard, T., Gudmundsdóttir, S., Studt, F., Rossmeisl, J., Abild-Pedersen, F., Vegge, T., Jónsson, H., and Nørskov, J.K. (2012). A theoretical evaluation of possible transition metal electro-catalysts for N2 reduction. Phys. Chem. Chem. Phys. *14*, 1235–1245. https://doi.org/10.1039/c1cp22271f.
8. Stoukides, M., and Vayenas, C.G. (1981). The effect of electrochemical oxygen pumping on the rate and selectivity of ethylene oxidation on polycrystalline silver. J. Catal. *70*, 137–146. https://doi.org/10.1016/0021-9517(81)90323-7.
9. Blanck, P., Martin, E.P., Schmider, D., Kee, R.J., Dailly, J., and Deutschmann, O. (2025). Electrochemical Ammonia Synthesis in a Proton-Conducting Ceramic Cell: A Parameter Study of an Iron-Based Electrode. J. Electrochem. Soc. *172*, 084507. https://doi.org/10.1149/1945-7111/adfc9e.
10. Li, C.-I., Matsuo, H., and Otomo, J. (2021). Kinetic and deuterium isotope analyses of ammonia electrochemical synthesis. RSC Adv. *11*, 17891–17900. https://doi.org/10.1039/D1RA00190F.
11. Otomo, J., Noda, N., and Kosaka, F. (2015). Electrochemical Synthesis of Ammonia with Proton Conducting Solid Electrolyte Fuel Cells at Intermediate Temperatures. ECS Trans. *68*, 2663–2670. https://doi.org/10.1149/06801.2663ecst.
12. Kobayashi, Y., Shimoda, N., Kimura, Y., and Satokawa, S. (2017). Electrochemical Synthesis of Ammonia Using Proton Conducting Solid Electrolyte and Ru-doped $BaCe_{0.9}Y_{0.1}O_{3-\delta}$ Electrode Catalyst. ECS Trans. *75*, 43–52. https://doi.org/10.1149/07542.0043ecst.
13. Klinsrisuk, S., and Irvine, J.T.S. (2017). Electrocatalytic ammonia synthesis via a proton conducting oxide cell with $BaCe_{0.5}Zr_{0.3}Y_{0.16}Zn_{0.04}O_{3-\delta}$ electrolyte membrane. Catal. Today *286*, 41–50. https://doi.org/10.1016/j.cattod.2016.06.051.
14. Kosaka, F., Nakamura, T., and Otomo, J. (2017). Electrochemical Ammonia Synthesis Using Mixed Protonic-Electronic Conducting Cathodes with Exsolved Ru-Nanoparticles in Proton Conducting Electrolysis Cells. J. Electrochem. Soc. *164*, F1323–F1330. https://doi.org/10.1149/2.0401713jes.
15. Li, C.-I., Oikawa, A., Kosaka, F., and Otomo, J. (2019). Electrochemical promotion of ammonia synthesis with proton-conducting solid oxide fuel cells. Adv. Mater. Lett. *10*, 563–568. https://doi.org/10.5185/amlett.2019.2259.

16. Kim, H., Chung, Y.S., Kim, T., Yoon, H., Sung, J.G., Jung, H.K., Kim, W.B., Sammes, L.B., and Chung, J.S. (2019). Ru-doped barium strontium titanates of the cathode for the electrochemical synthesis of ammonia. Solid State Ionics *339*, 115010. https://doi.org/10.1016/j.ssi.2019.115010.

17. Li, M., Hua, B., Wu, W., Wang, L.-C., Ding, Y., Welander, M.M., Walker, R.A., and Ding, D. (2022). Activating nano-bulk interplays for sustainable ammonia electrosynthesis. Mater. Today *60*, 31–40. https://doi.org/10.1016/j.mattod.2022.09.011.

18. Weng, G., Lei, S., Wang, R., Ouyang, K., Dong, J., Lin, X., Xue, J., Ding, L.-X., and Wang, H. (2023). A high-efficiency electrochemical proton-conducting membrane reactor for ammonia production at intermediate temperatures. Joule *7*, 1333–1346. https://doi.org/10.1016/j.joule.2023.05.013.

19. Kamitani, N., Jeong, S., Habazaki, H., and Aoki, Y. (2024). Vanadium Nitride Is an Efficient Hydrogen-Diffusive Cathode for Green Ammonia Electrochemical Synthesis by Protonic Solid Oxide Electrolysis Cells. ACS Sustainable Chem. Eng. *12*, 2100–2109. https://doi.org/10.1021/acssuschemeng.3c07736.

20. Chen, J., Gao, W., Zhu, L., Tao, H., Feng, S., Cao, H., Guo, J., Chen, Y., and Chen, P. (2024). A mixed proton-electron-conducting cathode with a Ru nanoparticle catalyst for electrochemical ammonia synthesis based on a proton-conducting BZCYYb electrolyte. J. Mater. Chem. A *12*, 26667–26677. https://doi.org/10.1039/D4TA04520C.

21. Dang, H., and Wang, E. (2025). Efficient ammonia synthesis in perovskite cathode-supported protonic ceramic electrochemical cell with dendritic porous structure. Ceram. Int. *51*, 18841–18851. https://doi.org/10.1016/j.ceramint.2025.02.063.

22. Lei, Z., Jing, J., Pang, J., Hu, R., Shi, X., Yang, Z., and Peng, S. (2020). Highly conductive proton-conducting electrolyte with a low sintering temperature for electrochemical ammonia synthesis. Int. J. Hydrogen Energy *45*, 8041–8051. https://doi.org/10.1016/j.ijhydene.2020.01.039.

23. Yuan, Y., Tada, S., and Kikuchi, R. (2022). Electrochemically promoted ammonia synthesis on an Fe/$BaZr_{0.8}Y_{0.2}O_{3-\delta}$ catalyst at ambient pressure. Sustain. Energy Fuels *6*, 458–465. https://doi.org/10.1039/D1SE01712H.

24. Kyriakou, V., Garagounis, I., Vourros, A., Vasileiou, E., and Stoukides, M. (2020). An Electrochemical Haber-Bosch Process. Joule *4*, 142–158. https://doi.org/10.1016/j.joule.2019.10.006.

25. Okazaki, M., and Otomo, J. (2022). Iron-Based Electrode Structures for Ammonia Electrosynthesis Cells with Proton-Conducting Ceramic Electrolytes. ECS Trans. *109*, 3–12. https://doi.org/10.1149/10913.0003ecst.

26. Li, C.-I., Matsuo, H., and Otomo, J. (2021). Effective electrode design and the reaction mechanism for electrochemical promotion of ammonia synthesis using Fe-based electrode catalysts. Sustain. Energy Fuels *5*, 188–198. https://doi.org/10.1039/D0SE01385D.

27. Okazaki, M., and Otomo, J. (2024). Ceria-iron electrocatalysts for ammonia electrosynthesis using protonic ceramic electrolysis cells. Solid State Ionics *414*, 116649. https://doi.org/10.1016/j.ssi.2024.116649.

28. Kosaka, F., Nakamura, T., Oikawa, A., and Otomo, J. (2017). Electrochemical Acceleration of Ammonia Synthesis on Fe-Based Alkali-Promoted Electrocatalyst with Proton Conducting Solid Electrolyte. ACS Sustainable Chem. Eng. *5*, 10439–10446. https://doi.org/10.1021/acssuschemeng.7b02469.

29. Guo, W., Li, Y., Li, S.-D., Shao, Z., and Chen, H. (2024). Ammonia synthesis *via* a protonic ceramic electrolysis cell (PCEC) using $LaCu_{0.1}Fe_{0.9}O_{3-\delta}$ catalyst. J. Mater. Chem. A *12*, 1200–1210. https://doi.org/10.1039/D3TA04559E.

30. Okazaki, M., and Otomo, J. (2024). Electrochemical Promotion of Ammonia Synthesis Integrated Directly with Steam Electrolysis. Ind. Eng. Chem. Res. *63*, 17413–17418. https://doi.org/10.1021/acs.iecr.4c02192.

31. Okazaki, M., and Otomo, J. (2023). Electrode-Supported Protonic Ceramic Electrolysis Cells for Electrochemically Promoted Ammonia Synthesis at Intermediate Temperatures. ACS Omega *8*, 40299–40308. https://doi.org/10.1021/acsomega.3c04478.

32. O. Deutschmann, DETCHEM Software Package, 2.9 ed., www.detchem.com, Karlsruhe 2022.

33. Hagen, S., Barfod, R., Fehrmann, R., Jacobsen, C.J.H., Teunissen, H.T., Ståhl, K., and Chorkendorff, I. (2002). New efficient catalyst for ammonia synthesis: barium-promoted cobalt on carbon. Chem. Commun. *38*, 1206–1207. https://doi.org/10.1039/b202781j.

34. Humphreys, J., Lan, R., and Tao, S. (2021). Development and Recent Progress on Ammonia Synthesis Catalysts for Haber–Bosch Process. Adv. Energy Sustain. Res. *2*, 2000043. https://doi.org/10.1002/aesr.202000043.

35. Yan, P., Guo, W., Liang, Z., Meng, W., Yin, Z., Li, S., Li, M., Zhang, M., Yan, J., Xiao, D., et al. (2019). Highly efficient K-Fe/C catalysts derived from metal-organic frameworks towards ammonia synthesis. Nano Res. *12*, 2341–2347. https://doi.org/10.1007/s12274-019-2349-0.

36. Fan, H., Huang, X., Kähler, K., Folke, J., Girgsdies, F., Teschner, D., Ding, Y., Hermann, K., Schlögl, R., and Frei, E. (2017). In-Situ Formation of Fe Nanoparticles from FeOOH Nanosheets on γ-Al_2O_3 as Efficient Catalysts for Ammonia Synthesis. ACS Sustainable Chem. Eng. *5*, 10900–10909. https://doi.org/10.1021/acssuschemeng.7b02812.

37. Garagounis, I., Vourros, A., Stoukides, D., Dasopoulos, D., and Stoukides, M. (2019). Electrochemical Synthesis of Ammonia: Recent Efforts and Future Outlook. Membranes *9*, 112. https://doi.org/10.3390/membranes9090112.

38. Lin, B., Guo, Y., Cao, C., Ni, J., Lin, J., and Jiang, L. (2018). Carbon support surface effects in the catalytic performance of Ba-promoted Ru catalyst for ammonia synthesis. Catal. Today *316*, 230–236. https://doi.org/10.1016/j.cattod.2018.01.008.

39. Luz, I., Parvathikar, S., Carpenter, M., Bellamy, T., Amato, K., Carpenter, J., and Lail, M. (2020). MOF-derived nanostructured catalysts for low-temperature ammonia synthesis. Catal. Sci. Technol. *10*, 105–112. https://doi.org/10.1039/C9CY01303B.

40. Fang, H., Liu, D., Luo, Y., Zhou, Y., Liang, S., Wang, X., Lin, B., and Jiang, L. (2022). Challenges and Opportunities of Ru-Based Catalysts toward the Synthesis and Utilization of Ammonia. ACS Catal. *12*, 3938–3954. https://doi.org/10.1021/acscatal.2c00090.

41. Li, L., Zhang, T., Cai, J., Cai, H., Ni, J., Lin, B., Lin, J., Wang, X., Zheng, L., Au, C.-T., and Jiang, L. (2020). Operando spectroscopic and isotopic-label-directed observation of LaN-promoted Ru/ZrH_2 catalyst for ammonia synthesis via associative and chemical looping route. J. Catal. *389*, 218–228. https://doi.org/10.1016/j.jcat.2020.05.039.

42. Sekine, Y. (2023). Low temperature ammonia synthesis by surface protonics over metal supported catalysts. Faraday Discuss. *243*, 179–197. https://doi.org/10.1039/D2FD00146B.

43. Hisai, Y., Ma, Q., Qureishy, T., Watanabe, T., Higo, T., Norby, T., and Sekine, Y. (2021). Enhanced activity of catalysts on substrates with surface protonic current in an electrical field – a review. Chem. Commun. *57*, 5737–5749. https://doi.org/10.1039/D1CC01551F.

44. Blanck, P., Schmider, D., Kee, R.J., Dailly, J., and Deutschmann, O. (2025). Microstructural optimizations of an iron-containing electrode for electrochemical ammonia synthesis on a proton-conducting ceramic membrane. Ceram. Int. *51*, 34213–34222. https://doi.org/10.1016/j.ceramint.2025.05.149.

45. Prudenziati, M., Morten, B., and Travan, E. (2003). Reduction process of RuO_2 powders and kinetics of their re-oxidation. Mater. Sci. Eng., B *98*, 167–176. https://doi.org/10.1016/s0921-5107(03)00049-7.